

Efficient method for approximating nonlinear dynamics: applications to uncertainty propagation and estimation

Javier Roa* and Ryan S. Park†

Jet Propulsion Laboratory, California Institute of Technology, Pasadena, CA, 91109

High-order Taylor series expansions can be used to model nonlinear dynamics at the cost of integrating a large set of variational equations to obtain high-order state-transition tensors (STTs). This paper presents an innovative technique for approximating the high-order STTs that reduces significantly the computational cost by retaining only the dominant secular terms. We propagate the low-order partial derivatives of Kepler’s equation, which only requires the integration of six additional equations to extend an n -th order approximation to order $(n+1)$. The approximation stems from the Lindstedt-Poincaré procedure and exploits the stability properties of orbital motion. Since the method makes no dynamical assumptions, it can accommodate any source of orbital perturbations. We show how the approximation of the second-order STT significantly increases the accuracy of the linear method for uncertainty propagation with only a small computational overhead. Finally, we derive a high-order approximate extended Kalman filter that implements the proposed approximation of the STT and improves the performance of linear filters. Examples of application with different perturbation sources include the heliocentric orbit of an asteroid, an orbiter around Europa, and an Earth-orbiting satellite.

I. Introduction

DIFFERENT methods for nonlinear orbit uncertainty propagation are available in the literature. Monte Carlo (MC) sampling relies on the individual propagation of a set of trajectories whose initial conditions are drawn from the initial distribution of orbital uncertainty. The unscented transform [1, 2] reduces the computational cost of MC sampling by propagating only a few special points (called *sigma* points) that are judiciously chosen to represent the first and second moments of the posterior distribution. Other techniques like Gaussian mixture models [3], which decompose the uncertainty domain into separate Gaussian distributions that are propagated independently, or polynomial chaos [4], which seeks polynomial approximations of the uncertainty region that are then propagated over time, present attractive alternatives to sampling methods. Taylor series expansions model the dynamics in the vicinity of the nominal trajectory and retaining high-order terms can also represent the nonlinear evolution of the uncertainty distribution [5].

Different uncertainty propagation techniques produce different estimation filters; for example, particle filters utilize MC sampling to map the posterior distribution [6], the unscented Kalman filter improves upon the extended Kalman filter by propagating the moments of the uncertainty distribution using the unscented transform [2], and high-order Taylor series expansions yield nonlinear Kalman filters [7].

Expansions in Taylor series are particularly useful for uncertainty propagation and estimation because they provide useful insights about the evolution of neighboring trajectories. In addition, most orbit propagation programs return not only the state but also the first-order partial derivatives of the state (i.e., the state-transition matrix or STM), which already constitute the first-order terms of the series. The main drawback of implementing high-order series expansions for uncertainty propagation is the complexity associated with the propagation of the high-order variational equations. For a system of dimension d , computing the terms of order p requires the integration of d^{p+1} additional differential equations to obtain the corresponding state-transition tensors (STTs).

Secular terms present in the series expansion are responsible for nonlinear effects accumulating over time. The Lindstedt-Poincaré method aims at eliminating secular terms from series solutions by introducing an angle-like independent variable that replaces physical time [8, pp. 54–60]. In the context of regularization in orbital mechanics, it became apparent that introducing an independent variable different from physical time via the more general Sundman transformation could also improve the performance of orbit propagation algorithms [9, 10], often significantly. Details on the propagation of the variational equations using regularized formulations can be found in Ref. [11].

*Navigation Engineer, Solar System Dynamics Group, 4800 Oak Grove Dr, Pasadena, CA 91109. javier.roa@jpl.nasa.gov

†Group Supervisor, Solar System Dynamics Group, 4800 Oak Grove Dr, Pasadena, CA 91109.

©2020 California Institute of Technology. Government sponsorship acknowledged.

In the present paper, we develop a technique for approximating high-order STTs by identifying the dominant secular terms. Secular terms are isolated by introducing a change of variable similar to Sundman's transformation. Thanks to retaining just the most relevant terms, the approximation requires the computation of only a small fraction of the all the terms that form the actual STT. For example, only seven additional equations instead of 216 are needed to approximate the second-order STT. The approximation accommodates any orbital perturbation that may be included in the model. Numerical results indicate that Taylor series using the approximate STTs are more than one order of magnitude more accurate than the linear approximation, and the overhead in computational cost is small. Finally, we implement the proposed approximation into a high-order Kalman filter to improve the performance of the estimation compared to the extended Kalman filter.

II. Variational equations

Let $\mathbf{x} \in \mathbb{R}^d$ denote the state vector of a dynamical system whose evolution may depend on a set of physical parameters $\boldsymbol{\xi} \in \mathbb{R}^\ell$, which we assume to be constant. In this paper, we take $d = 6$ but the formulation could be generalized if needed. Concatenating both vectors produces the extended state vector $\mathbf{y} \in \mathbb{R}^{6+\ell}$. The system abides by the differential equation

$$\frac{d\mathbf{y}}{dt} = \mathbf{f}(t; \mathbf{y}), \quad \mathbf{y}(t^o) = \mathbf{y}^o. \quad (1)$$

The superscript o denotes variables expressed at the initial time. Equation (1) can be integrated either analytically or numerically to describe the time evolution of the system:

$$\mathbf{y}(t) \equiv \mathbf{F}(t; \mathbf{y}^o) = \int_{t^o}^t \mathbf{f}(t; \mathbf{y}) dt. \quad (2)$$

We focus on periodic and almost periodic dynamical systems that satisfy

$$\|\mathbf{y}(t^o + nT) - \mathbf{y}(t^o)\| < \delta, \quad (3)$$

where $T > 0$ is the period of the oscillation and $n \in \mathbb{N}$ is an arbitrary number of revolutions. The tolerance δ is assumed to be small and perfectly periodic motions are characterized by $\delta \rightarrow 0$. From now on we particularize the discussion to the perturbed two-body problem where Eq. (1) takes the form

$$\frac{d\mathbf{y}}{dt} = \begin{bmatrix} \mathbf{v} \\ -\frac{\mu}{r^3} \mathbf{r} + \mathbf{a}_p \\ \mathbf{0}_{\ell \times 1} \end{bmatrix} \quad (4)$$

written in terms of the position (\mathbf{r}), velocity (\mathbf{v}), and perturbation (\mathbf{a}_p) vectors. The solution for Keplerian motion ($\mathbf{a}_p = 0$) is perfectly periodic whereas weak orbital perturbations lead to almost-periodic trajectories.

A. Series expansion

One approach to propagating the uncertainty distribution associated with the initial conditions \mathbf{y}^o is to characterize the evolution of neighboring trajectories that are initially close to the nominal. Given a neighboring trajectory \mathbf{y}' , the deviation with respect to the nominal trajectory, $\delta\mathbf{y}(t)$, follows from particularizing Eq. (2) at the nominal and the neighboring trajectories:

$$\delta\mathbf{y}(t) = \mathbf{F}(t; \mathbf{y}^o + \delta\mathbf{y}^o) - \mathbf{F}(t; \mathbf{y}^o). \quad (5)$$

Under the assumption that the initial deviation ($\delta\mathbf{y}^o$) is small compared to the initial conditions, $\|\delta\mathbf{y}^o\|/\|\mathbf{y}^o\| \sim \varepsilon \ll 1$, this expression can be expanded in Taylor series using Einstein's tensor notation* like [5]

$$\delta y_i(t) = \Phi_{i,k_1}^{(t^o,t)} \delta y_{k_1}^o + \frac{1}{2!} \Phi_{i,k_1 k_2}^{(t^o,t)} \delta y_{k_1}^o \delta y_{k_2}^o + \dots \quad (6)$$

The first term $\Phi_{i,k_1}^{(t^o,t)}$ is the STM of the system, which captures the linear variations of the integral flow (2) from time t^o through time t . Similarly, $\Phi_{i,k_1 k_2}^{(t^o,t)}$ is the second-order STT comprised of the second-order derivatives of the flow. In its

*Repeated indices indicate summation, e.g., $a_{ij}b_j \equiv \sum_j a_{ij}b_j$.

most general form up to order m , this expansion reads

$$\delta y_i(t) = \sum_{p=1}^m \frac{1}{p!} \Phi_{i,k_1 \dots k_p}^{(t^o, t)} \delta y_{k_1}^o \dots \delta y_{k_p}^o + \mathcal{O}(\varepsilon^{m+1}). \quad (7)$$

The STT of any given order p takes the form:

$$\Phi_{i,k_1 \dots k_p}^{(t^o, t)} = \left. \frac{\partial^p F_i(t)}{\partial y_{k_1}^o \dots \partial y_{k_p}^o} \right|_t. \quad (8)$$

In some special scenarios the partial derivatives of the trajectory may be available analytically, although in most situations the STTs in Eq. (8) are evaluated numerically.

B. Secular terms

The accuracy of the expansion (7) degrades as secular terms grow over time. Secular terms stem from the fact that deviations on the initial conditions that change the period (or equivalently the natural frequency $\omega = 2\pi/T$) of the system produce Lyapunov unstable relative dynamics. Consider a nominal trajectory with period T and a neighboring trajectory with period $T' = T + \delta T$, where δT is a result of the deviation on the initial conditions $\delta \mathbf{y}^o$. After n revolutions along the nominal trajectory, the deviation will be

$$\delta \mathbf{y}(nT) = \mathbf{y}'(nT) - \mathbf{y}(nT) = \mathbf{y}'(n(T' - \delta T)) - \mathbf{y}(nT) \approx [\mathbf{y}'(nT') - \mathbf{y}(nT)] - n \frac{d\mathbf{y}'}{dt} \delta T + \dots \quad (9)$$

The difference $\mathbf{y}'(nT') - \mathbf{y}(nT)$ remains bounded (and small) as n increases because Eq. (3) holds for both the nominal and the deviated trajectory, which is T' -periodic. However, the last term of the expansion grows linearly with the number of revolutions n and results in a continuous drift in the mutual separation between trajectories.

The Lindstedt-Poincaré (LP) procedure suggests the introduction of the change of variable $t \mapsto \theta = \omega t$, where θ is an angular variable defined in terms of a fundamental frequency ω . Let us introduce a generalized LP change of variable given by the dynamical relation

$$\frac{d\theta}{dt} = \gamma(t; \mathbf{y}), \quad \theta^o = 0. \quad (10)$$

In this expression, γ needs not be constant or defined analytically as long as it is differentiable. The condition $\theta^o = 0$ can be met easily by adjusting the origin from which angles are measured. The angular variable θ is then given by the integral relation

$$\theta(t) \equiv \Theta(t; \mathbf{y}^o) = \int_{t^o}^t \gamma(t; \mathbf{y}) dt. \quad (11)$$

The most important effect of the change of variable is that the system becomes 2π -periodic when transcribed to the θ -domain. Eliminating the dependency of the period with the initial conditions translates into both the nominal and the perturbed trajectory having the same period in the transformed space, which results in an effective stabilization of the motion:

$$\|\delta \mathbf{y}(2n\pi)\| = \|\mathbf{y}'(2n\pi) - \mathbf{y}(2n\pi)\| \ll 1. \quad (12)$$

This result holds true for any number of revolutions n .

It should be noted that the time along the two trajectories, \mathbf{y}' and \mathbf{y} , will not be the same because it takes different amounts of time to traverse a given angular distance. The time difference between the two solutions in the θ -domain has been discussed in the literature using different terminology, including synchronous correspondence [12], contemporaneous variations [13], or asynchronous relative motion [14, 15].

C. Simplified computation of high-order state-transition tensors

Equation (8) defines the STT of order p in terms of the p -th partial derivatives of the integral flow with respect to the initial conditions at a given time. When introducing the change of variable $t \mapsto \theta$, it is convenient to rewrite the partial derivatives along the trajectory like:

$$\left. \frac{\partial \mathbf{F}}{\partial y_i^o} \right|_t = \left. \frac{\partial \mathbf{G}}{\partial y_i^o} \right|_\theta + \frac{\partial \Theta}{\partial y_i^o} \frac{d\mathbf{G}}{d\theta}, \quad (13)$$

where \mathbf{G} is just the representation of the flow in θ -space, $\mathbf{y}(\theta) = \mathbf{G}(\theta; \mathbf{y}^o)$. Thanks to this expression, the STT can be alternatively computed from

$$\Phi_{i,k_1\dots k_p}^{(t^o,t)} = \left(\frac{\partial}{\partial y_{k_1}^o} + \Gamma_{k_1} \frac{d}{d\theta} \right) \dots \left(\frac{\partial G_i}{\partial y_{k_p}^o} + \Gamma_{k_p} \frac{dG_i}{d\theta} \right). \quad (14)$$

For convenience, we introduced the notation

$$\Gamma_{k_1\dots k_p} = \frac{\partial^p \Theta}{\partial y_{k_1}^o \dots \partial y_{k_p}^o} \Big|_t. \quad (15)$$

Taking the partial derivative of Eq. (11) with respect to the initial conditions yields

$$\frac{\partial \Theta}{\partial y_i^o} = \int_{t^o}^t \frac{\partial \gamma}{\partial y_i^o} dt. \quad (16)$$

In general, this term contains secular terms that grow over time while the derivatives of \mathbf{G} oscillate. As an example, consider the simple case of $\gamma \equiv \omega$ constant. Equation (16) reduces to:

$$\frac{\partial \Theta}{\partial y_i^o} = \frac{\partial \omega}{\partial y_i^o} (t - t^o), \quad (17)$$

where $\partial \omega / \partial y_i^o$ is constant and hence $\partial \Theta / \partial y_i^o$ grows linearly with time.

After having identified the term Γ_{k_j} as the source of secular terms, it follows that the dominant secular terms of order $o(\varepsilon^p)$ in Eq. (7) are:

$$\Gamma_{k_1} \dots \Gamma_{k_p} \frac{d^p G_i}{d\theta^p} \delta y_{k_1}^o \dots \delta y_{k_p}^o \sim \varepsilon^p t^p \quad (18)$$

Note that the derivatives $d^p G_i / d\theta^p$ relate to Eq. (1) by means of:

$$\frac{d^p G_i}{d\theta^p} = \frac{1}{\gamma} \frac{d}{dt} \left(\frac{1}{\gamma} \frac{d}{dt} \left(\dots \frac{f_i}{\gamma} \right) \right) \quad (19)$$

Neglecting the contribution of the cross derivatives results in:

$$\frac{d^p G_i}{d\theta^p} \simeq \frac{1}{\gamma^p} \frac{d^{p-1} f_i}{dt^{p-1}}, \quad (20)$$

which means that the STT of order p can be approximated like

$$\Phi_{i,k_1\dots k_p} \simeq \Gamma_{k_1} \dots \Gamma_{k_p} \frac{1}{\gamma^p} \frac{d^{p-1} f_i}{dt^{p-1}}. \quad (21)$$

The main advantage of this approximation over the computation of the p -th order STT is that the only partial derivatives that need to be computed are the $6 + \ell$ terms in Γ_{k_j} (ℓ is the number of physical parameters), compared to the $(6 + \ell)^p$ derivatives involved in the computation of the exact STT. This translates into a significant speedup since computing each partial derivative requires the integration of one additional equation.

D. Accuracy of the approximation

Equation (21) is particularly useful for approximating the second-order STT to improve the accuracy of the linear expansion. First, the full STM is propagated to the desired time to obtain a first-order approximation of the solution. Then, adding the contribution of the second-order STT approximated with Eq. (21) improves the accuracy of the expansion thanks to accounting for the dominant nonlinear terms.

An STT of order p in the Taylor series expansion (7) contains secular terms that grow over time like t, t^2, \dots, t^p . For the case $p = 2$, there are only linear and quadratic terms proportional to t and t^2 , respectively. Consequently, the approximation (21) only neglects terms of order $\varepsilon^2 t$ and non-secular terms $o(\varepsilon^2)$. For short propagation times (up to $t \sim 1$), when the solution remains in the linear regime, the contribution from the STT of order $p = 2$ will be small

compared to the linear terms meaning that, even though all the secular terms that conform the STT remain comparable in magnitude, their contribution is so small that neglecting some of them in the approximation does not affect the overall accuracy. Conversely, for long propagation times ($t \sim 1/\varepsilon$), terms proportional to $\varepsilon^2 t^2$ will be comparable to terms of order εt causing high-order nonlinear terms to become as important as linear terms. In this scenario, $o(\varepsilon^2 t^2) \gg o(\varepsilon^2 t) \gg o(\varepsilon^2)$ and therefore it is safe to neglect the terms that grow linearly with time or that are periodic.

Care should be taken when using Eq. (21) to approximate the STTs of several orders consecutively, e.g., $o(\varepsilon^p)$ and $o(\varepsilon^{p+1})$. The approximation captures only the terms proportional to t^p and t^{p+1} . This may be problematic because some of the cross-terms of order p that are being neglected (proportional to t^{p-1}, t^{p-2}, \dots) may become as important as the dominant terms of order $p+1$ as time grows. For this reason, including secular terms of several orders in ε using only the proposed approximation may require retaining additional terms in Eq. (14) to really notice an improvement over the p -th order approximation.

E. Practical implementation: approximation of the second-order STT

In this section, we present details on the implementation of the approximation of the STT of order two. First, we must provide the dynamical definition of $d\theta/dt$ in Eq. (10). In practice, we recommend defining θ as the true anomaly f except that the origin of angles is set at \mathbf{r}^o instead of at periapsis. This ensures that $\theta(t) = f(t) - f^o$ is zero at t^o and yields:

$$\frac{d\theta}{dt} \equiv \gamma = \frac{h}{r^2}, \quad \theta(t^o) = 0. \quad (22)$$

By simply appending θ to the vector of state and parameters, $\mathbf{y}^* = [\mathbf{y}, \theta]$, we arrive at the extended form of Eq. (4):

$$\frac{d\mathbf{y}^*}{dt} \equiv \mathbf{f}^*(t; \mathbf{y}^*) = \begin{bmatrix} \mathbf{v} \\ -(\mu/r^3)\mathbf{r} + \mathbf{a}_p \\ \mathbf{0}_{\ell \times 1} \\ h/r^2 \end{bmatrix} \quad (23)$$

The STM Φ associated with \mathbf{y}^* decomposes in four blocks:

$$\Phi^* = \begin{bmatrix} \left. \frac{\partial \mathbf{y}}{\partial \mathbf{y}^o} \right|_t & \mathbf{0} \\ \left. \frac{\partial \theta}{\partial \mathbf{y}^o} \right|_t & 1 \end{bmatrix}. \quad (24)$$

Its time evolution follows from integrating the first-order variational equations in the usual way:

$$\frac{d\Phi^*}{dt} = \mathbf{A}^* \Phi^*, \quad \Phi^*(t^o) = \mathbf{I}, \quad (25)$$

using the Jacobian

$$\mathbf{A}^* = \frac{\partial \mathbf{f}^*}{\partial \mathbf{y}^*}. \quad (26)$$

The partial derivatives of $\gamma = h/r^2$ defining the last row of the Jacobian are given by:

$$\frac{\partial \gamma}{\partial \mathbf{r}} = \frac{\gamma}{h} \frac{\partial h}{\partial \mathbf{r}} - \frac{2h}{r^4} \mathbf{r}^\top = +\frac{1}{r^2 h} (\mathbf{v} \times \mathbf{h})^\top - \frac{2h}{r^4} \mathbf{r}^\top \quad (27)$$

$$\frac{\partial \gamma}{\partial \mathbf{v}} = \frac{\gamma}{h} \frac{\partial h}{\partial \mathbf{v}} = -\frac{1}{r^2 h} (\mathbf{r} \times \mathbf{h})^\top \quad (28)$$

The last column of Φ^* is constant and it can be obviated during the integration to reduce the dimension of the system. Once Eqs. (23) and (25) have been integrated up to the desired time t , Eq. (21) can be applied directly to construct an approximation of the second-order STT:

$$\Phi_{i,ab}^{(t^o,t)} = \frac{r^4}{h^2} \frac{d^2 F_i}{dt^2} \frac{\partial \theta}{\partial y_a^o} \frac{\partial \theta}{\partial y_b^o} \quad (29)$$

where the derivatives $\partial\Theta/\partial y_j^o$ are contained in the last row of Φ^* —see Eq. (24)—. The second time derivative of the solution \mathbf{F} reduces to the acceleration \mathbf{a} and its time derivative, the jerk $\dot{\mathbf{a}}$:

$$\frac{d^2\mathbf{F}}{dt^2} = \begin{bmatrix} \mathbf{a} \\ \dot{\mathbf{a}} \end{bmatrix} \quad (30)$$

having obviated the null terms associated with the parameters ξ . The Appendix presents analytic expressions for the second-order derivatives of the acceleration, including perturbations.

The second-order approximation of the state is then given by:

$$\delta y_i(t) = \Phi_{i,a}^{(t^o,t)} \delta y_a^o + \frac{1}{2} \Phi_{i,ab}^{(t^o,t)} \delta y_a^o \delta y_b^o. \quad (31)$$

where the STM $\Phi^{(t^o,t)}$ is given by Eq. (25) and the STT is approximated by Eq. (29).

Ignoring momentarily the physical parameters ξ , implementing the approximation of the second-order STT requires the integration of six equations of state plus one extra equation for the angle θ , and 6×6 equations for the STM plus another six for the partials of Θ . In total, 49 equations need to be integrated to propagate the approximation of the second-order expansion. This is only seven additional equations compared to the $6 + 36 = 42$ equations required by the first-order expansion, and 209 fewer equations than the $6 + 36 + 216 = 258$ required by the complete second-order expansion. Furthermore, integrating the equation for $d\theta/dt$ is not strictly required and could be obviated for efficiency, although including it simplifies the implementation.

F. Example: propagation of neighboring trajectories based on the orbit of asteroid 2018 KS

As an example of application, consider the heliocentric orbit of the near-Earth asteroid 2018 KS whose osculating orbital elements are listed in Table 1. Our goal is to propagate the relative dynamics of a trajectory that is initially close to the nominal and compare the accuracy of the linear expansion (order $m = 1$) with the approximation of the second-order expansion ($m = 2$) presented in the previous section. The dynamical model includes the third-body perturbations from Earth, the Moon, and Jupiter. The initial conditions of the neighboring trajectory relative to the nominal orbit at the osculating epoch are $\delta \mathbf{r} = [1, 1, 1]$ km and $\delta \mathbf{v} = [10, 10, 10]$ mm/s, both expressed in the ecliptic ICRF/J2000 frame. The orbit is propagated forward in time for 10 revolutions (approximately 10 years).

Table 1 Osculating heliocentric orbital elements of the asteroid 2018 KS at epoch 2019-Aug-17 referred to the ICRF/J2000 frame using the ecliptic and mean equinox coordinate system.

a (au)	e	i (deg)	Ω (deg)	ω (deg)	M (deg)
1.006	0.1998	8.8607	59.4717	284.969	0

Figure 1 compares the accuracy of the linear and approximate second-order expansion by measuring the error in position and velocity with respect to the numerical propagation of the neighboring trajectory. The propagation based on the second order STT reduces the error by more than one order of magnitude, approximately by a factor of 50, both in position and velocity. The derivative of the acceleration including the third-body perturbation is computed using the expressions in the Appendix.

III. Nonlinear propagation of orbital uncertainty

A. General theory

Let the vector of state and parameters $\mathbf{y} \in \mathbb{R}^n$ ($n = 6 + \ell$) now be a Gaussian random vector $\mathbf{y} = \mathcal{N}(\mathbf{m}, \mathbf{P})$, with mean value \mathbf{m} and covariance matrix \mathbf{P} . The probability density function (PDF) associated with this distribution is

$$p(\mathbf{y}) = \frac{1}{\sqrt{(2\pi)^n \det(\mathbf{P})}} \exp \left[-\frac{1}{2} (\mathbf{y} - \mathbf{m})^\top \mathbf{P}^{-1} (\mathbf{y} - \mathbf{m}) \right]. \quad (32)$$

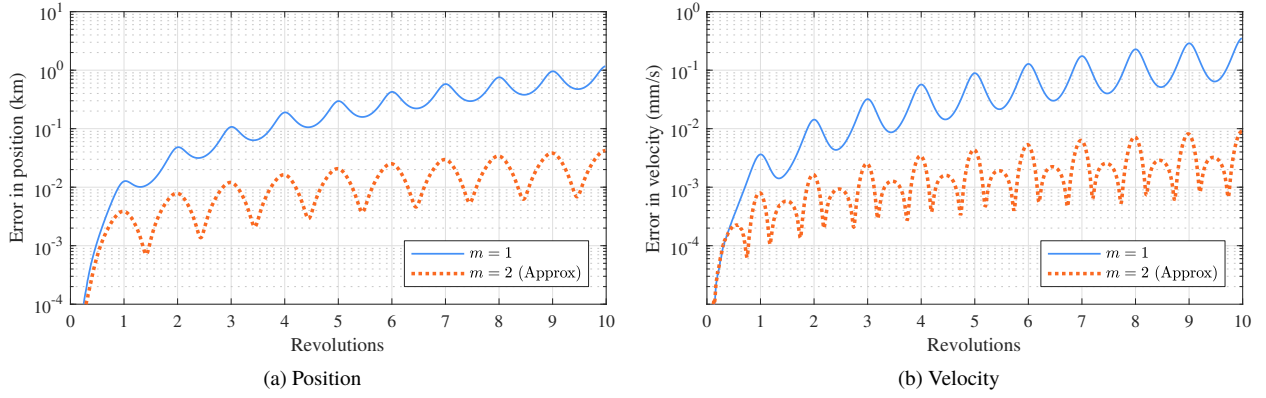


Fig. 1 Error in the propagation of the relative dynamics with respect to the orbit of asteroid 2018 KS.

Gaussian probability distributions are characterized by their first and second moments (mean and variance), which in turn can be defined in terms of the expectations:

$$\mathbb{E}[x_i] = m_i \quad (33)$$

$$\mathbb{E}[x_i x_j] = m_i m_j + P_{ij} \quad (34)$$

$$\mathbb{E}[x_i x_j x_k] = m_i m_j m_k + m_i P_{jk} + m_j P_{ik} + m_k P_{ij} \quad (35)$$

$$\begin{aligned} \mathbb{E}[x_i x_j x_k x_\ell] = & m_i m_j m_k m_\ell + P_{ij} P_{k\ell} + P_{ik} P_{j\ell} + P_{i\ell} P_{jk} + m_i m_j P_{k\ell} + m_i m_k P_{j\ell} \\ & + m_i m_\ell P_{jk} + m_j m_k P_{i\ell} + m_j m_\ell P_{ik} + m_k m_\ell P_{ij} \end{aligned} \quad (36)$$

According to the definition of the expectation in terms of the Lebesgue integral:

$$\mathbb{E}[\mathbf{x}(t)] = \int_{\infty} \mathbf{x}(t) p(t; \mathbf{x}) d\mathbf{x}, \quad (37)$$

the moments of the distribution can be propagated over time using the Taylor series approximation introduced in Eq. (7):

$$\delta m_i(t) = \sum_{p=1}^m \frac{1}{p!} \Phi_{i,k_1 \dots k_p} \mathbb{E}[\delta x_{k_1}^o \dots \delta x_{k_p}^o] \quad (38)$$

$$P_{ij}(t) = \left(\sum_{p=1}^m \sum_{q=1}^m \frac{1}{p!q!} \Phi_{i,k_1 \dots k_p} \Phi_{j,\ell_1 \dots \ell_q} \mathbb{E}[\delta x_{k_1}^o \dots \delta x_{k_p}^o \delta x_{\ell_1}^o \dots \delta x_{\ell_q}^o] \right) - \delta m_i \delta m_j \quad (39)$$

In this expression, $\delta \mathbf{m}$ denotes the mean of the deviation. In general, moments up to order $2m$ are required to propagate the covariance matrix via an expansion of order m .

Under the assumption that the initial deviation is zero, the second order expansion $m = 2$ simplifies to [5]:

$$\delta m_i(t) = \frac{1}{2} \Phi_{i,ab} P_{ab}^o \quad (40)$$

$$P_{ij}(t) = \Phi_{i,a} \Phi_{j,b} P_{aa}^o - \delta m_i \delta m_j + \frac{1}{4} \Phi_{i,ab} \Phi_{j,\alpha\beta} [P_{ab}^o P_{\alpha\beta}^o + P_{a\alpha}^o P_{b\beta}^o + P_{a\beta}^o P_{b\alpha}^o] \quad (41)$$

The linear approximation assumes that the mean always coincides with the reference trajectory (i.e. $\delta \mathbf{m}(t) = 0$), whereas mappings of higher order adequately capture the dynamics of the mean. This clearly indicates that introducing terms of second order, even if approximate, will produce a substantial improvement in the propagation of the first moments of the distribution.

B. Examples

1. Asteroid 2018 KS

Consider the orbit of asteroid 2018 KS defined in Table 1. Before propagating the moments of the distribution associated with the actual orbit uncertainty using Eqs. (40–41), we simulate the propagation of a simplified uncertainty domain by independently propagating a string of samples placed along the boundary of a simulated two-dimensional projection of the uncertainty region. In particular, we generate a set of samples forming a circular pattern on the orbital plane with radius $7 \times 10^{-6} a^o \simeq 10^3$ km and centered at the initial position, keeping the velocity equal to the nominal. Figure 2 depicts the initial pattern. The samples are then propagated over time using the linear and the second-order method and Fig. 2 presents the state of the simulated uncertainty domain at every other revolution. To simplify the visualization of the result, the solution is represented in the $x'y'$ -axes, which are contained on the orbital plane and x' is aligned with the major axis of the pattern predicted by the linear expansion. The unit of length is the initial value of the semimajor axis, a^o .

The predictions by the linear and second-order methods are compared with the numerical propagation of each individual sample. The second order method adequately captures the nonlinear behavior of the uncertainty region whereas the linear approximation fails to capture its curvature. As time progresses, this effect becomes more noticeable as the curvature of the uncertainty domain increases. It is important to note that the failure of the linear approach to capture the shape of the domain will also result in an error in the estimation of the mean.

Equations (40) and (41) provide an approximation truncated to order $m = 2$ of the first and second moments of the probability distribution at time t . To assess the accuracy of the propagation, these results can be compared with the

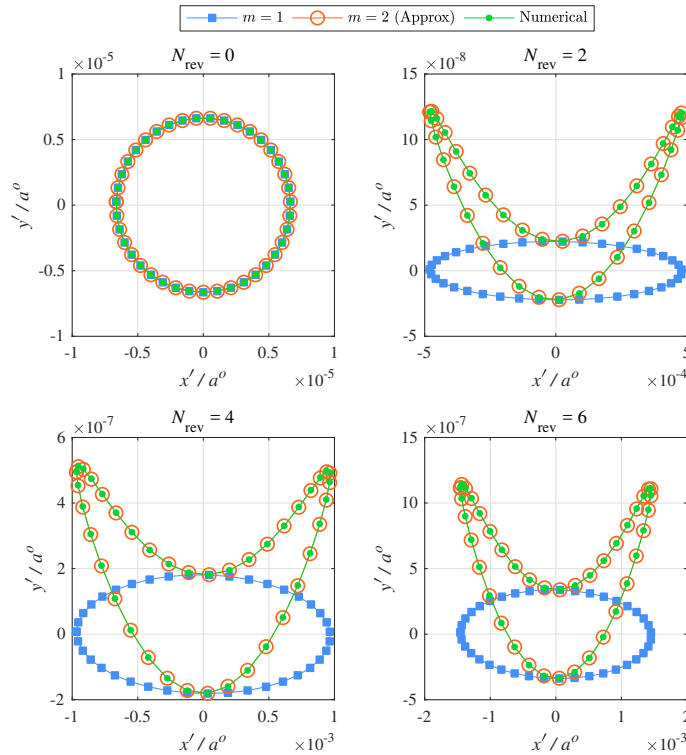


Fig. 2 Evolution of a fictitious uncertainty domain of asteroid 2018 KS according to the linear and second-order expansions, compared with the numerical integration of each sample.

predictions from a Monte Carlo (MC) propagation of N samples, $\{\tilde{\mathbf{y}}^1, \dots, \tilde{\mathbf{y}}^N\}$:

$$m_i(t) = \frac{1}{N} \sum_{j=1}^N \tilde{y}_i^j(t), \quad \delta m_i(t) = m_i(t) - y_i(t) \quad (42)$$

$$P_{ij}(t) = \frac{1}{N-1} \sum_{k=1}^N [\tilde{y}_i^k(t) - m_i(t)][\tilde{y}_j^k(t) - m_j(t)] \quad (43)$$

Table 2 presents the $1\text{-}\sigma$ uncertainties of the orbital elements of asteroid 2018 KS. A total of 10^6 MC samples are generated from a normal distribution centered at the reference orbit using the uncertainties listed in the table and neglecting the correlation between terms. The samples are propagated for 10 revolutions and the mean and covariance predicted by Eqs. (40) and (41) are compared against the values obtained from the MC propagation.

Table 2 Uncertainty of the orbital elements of asteroid 2018 KS ($1\text{-}\sigma$) at the initial epoch.

σ_a (au)	σ_e	σ_i (deg)	σ_Ω (deg)	σ_ω (deg)	σ_M (deg)
2.8×10^{-5}	9.9×10^{-5}	4.8×10^{-3}	2.3×10^{-5}	3.1×10^{-3}	8.1×10^{-4}

Figure 3 displays the error in the propagation of the mean, both in position and velocity. The errors are normalized with the characteristic distance a^o and the characteristic velocity $\sqrt{\mu/a^o}$, respectively. The second-order approximation reduces the error in the propagation of the mean by about one order of magnitude after 10 revolutions and the gains in accuracy grow over time. The large error in the propagation of the mean when incorporating only the linear terms is due to the fact that this approach assumes that the initial deviation $\delta \mathbf{m}^o$ remains null throughout the propagation, as indicated by Eq. (40). The UT-estimate remains close to the second-order approximation during the whole propagation.

Figure 4 compares the propagation of the covariance ellipsoid after 10 revolutions using the linear and the second-order expansions, together with MC estimate and the estimate from the unscented transform (UT). The covariance ellipsoid is projected on the radial-tangential-normal (RTN) frame. The second-order approximation adequately captures the size, shape, orientation, and position in space compared to the nonlinear estimates provided by the MC and UT methods. The fact that the linear approximation underestimates the evolution of the mean causes a clear offset in the position of the covariance ellipsoid.

The additional cost of propagating the variational equations of the angle θ required to construct the second-order approximation and the evaluation of the additional transformations is small. In particular, for this example the

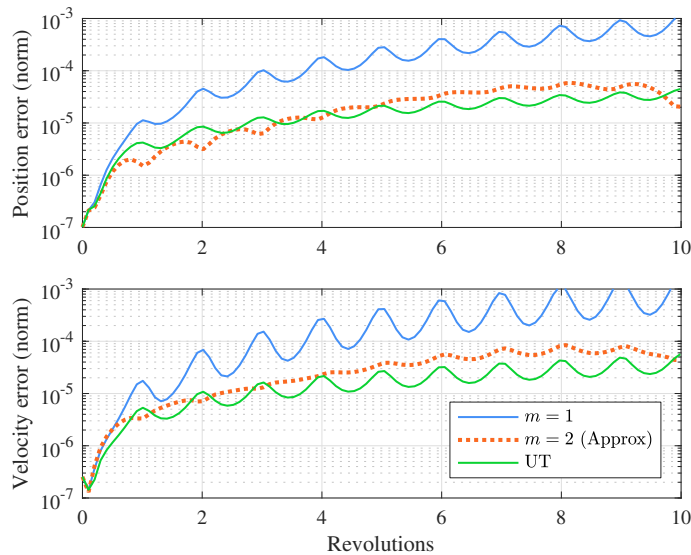


Fig. 3 Error in the propagation of the mean of the distribution of the orbit uncertainty of asteroid 2018 KS.

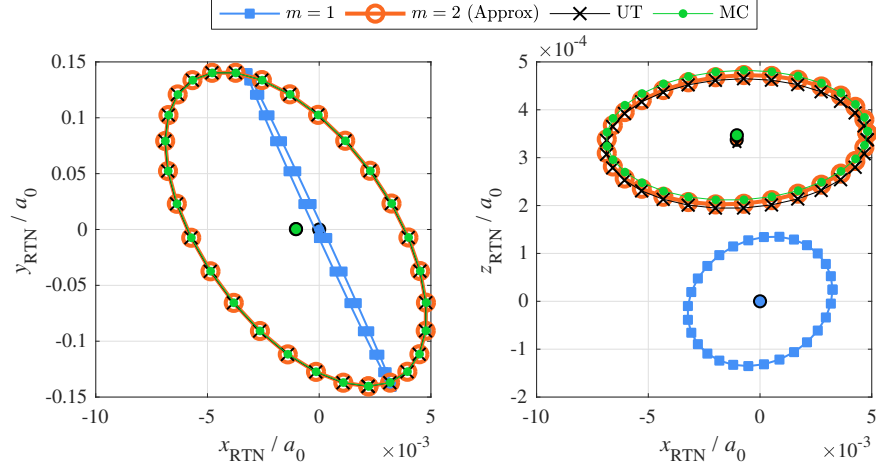


Fig. 4 Projection of the 3σ covariance ellipsoid of asteroid 2018 KS on the RTN frame after 10 revolutions.

computational time invested in evaluating the second-order approximation increased by only 5% compared to the purely linear expansion. The UT, on the other hand, requires the numerical propagation of 13 trajectories and resulted in a 280% increase in computational time compared to the linear approach. The simulations were run in Matlab using the ode45 integrator.

2. Spacecraft in low-Earth orbit

The second example of application is a spacecraft describing a low-Earth orbit (LEO) at an altitude of 500 km. Its orbital elements are listed in Table 3. The motion of the spacecraft is perturbed by the effect of Earth's oblateness and lunisolar tidal perturbations.

Table 3 Osculating orbital elements of a spacecraft in low-Earth orbit referred to the IAU76/J2000 geocentric equatorial frame (2018-Dec-14).

a (km)	e	i (deg)	Ω (deg)	ω (deg)	M (deg)
6871	0	70	30	20	0

First, we propagate over time a set of samples that initially form a circular pattern of radius 1 km using the linear and second-order methods. The solution is compared with the numerical integration of the orbit of each sample. Figure 5 displays the evolution of the uncertainty domain at every other revolution. Nonlinear effects stemming from the Keplerian shear cause the uncertainty to bend along the trajectory, producing a curvature that is accurately captured by the second-order solution.

Next, let us assume that the distribution of uncertainty of the spacecraft's orbit has zero mean and diagonal covariance with $\sigma_x = \sigma_y = \sigma_z = 1$ km and $\sigma_{v_x} = \sigma_{v_y} = \sigma_{v_z} = 0.1$ m/s. The mean of the distribution is propagated via Eq. (40) using the linear and second-order expansions. The error in the propagation of the mean (compared to the propagation of 10^6 MC samples) is presented in Fig. 6. The expansion of second order consistently improves the accuracy by over an order of magnitude compared to simply accounting for linear terms. The figure also includes the error in the estimation of the mean by the UT, which is comparable to the error obtained by the second-order approximation.

Finally, the covariance ellipsoid is propagated for 10 revolutions using Eq. (41) truncated to order first and second order and the resulting estimates are compared against the predictions of MC and UT sampling. The second-order approximation successfully captures the in-plane dynamics where the divergence is most prominent. There is a small offset in the out-of-plane projections of the covariance predicted by the UT and the second-order expansion when compared with MC sampling, with the maximum error reaching approximately 6% of the maximum out-of-plane excursion.

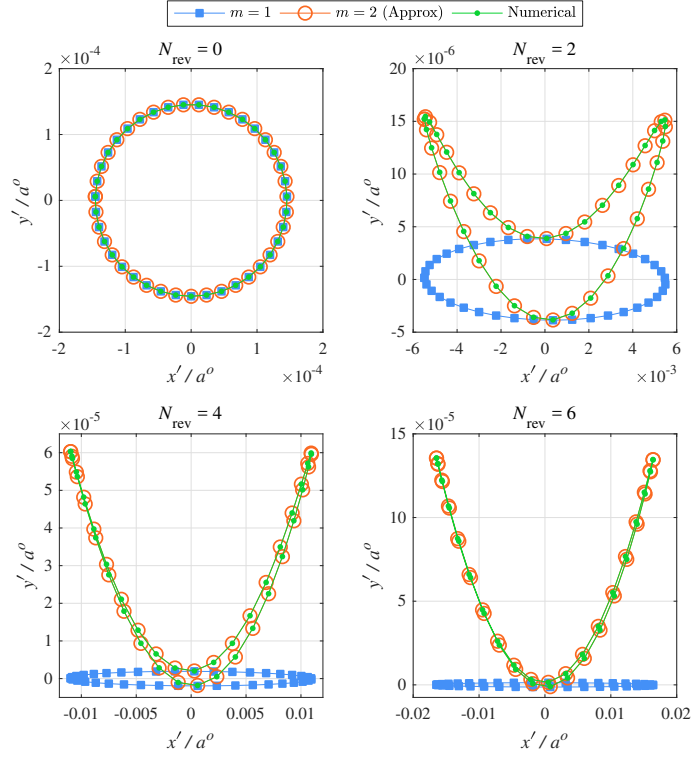


Fig. 5 Evolution of a fictitious uncertainty domain of a spacecraft in LEO according to the linear and second-order expansions, compared with the numerical integration of each sample.

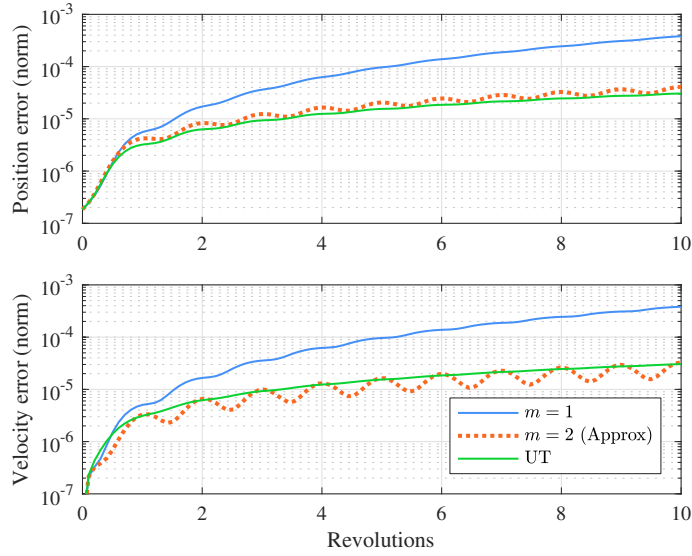


Fig. 6 Error in the propagation of the mean of the uncertainty distribution (spacecraft in LEO).

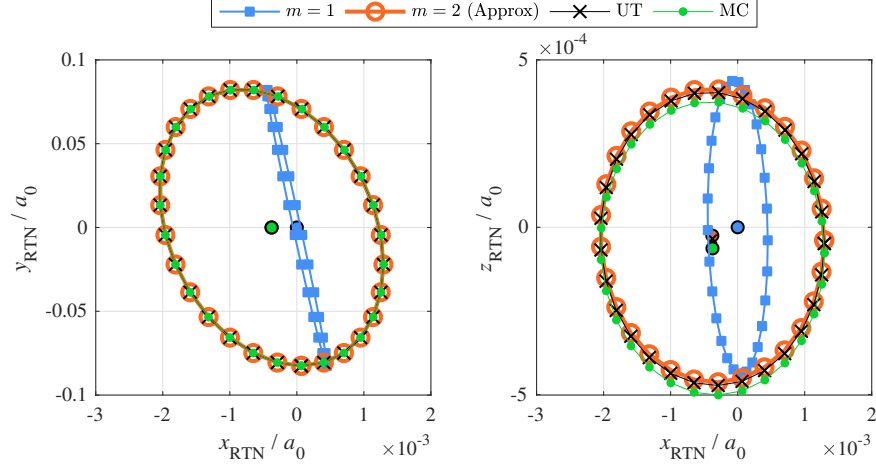


Fig. 7 Projection of the 3σ covariance ellipsoid of a spacecraft in LEO on the RTN frame after 10 revolutions.

The computational time in this example increased by 12% when propagating the second-order terms, whereas the UT required 270% more time than the linear method. As a result, the second-order approximation is as accurate as UT while being three times faster.

IV. Nonlinear estimation filter

In real scenarios, the deterministic trajectory solution in Eq. (2) is extended to account for the process noise $\mathbf{w}(t)$ that affects the dynamics or the knowledge of the physical parameters:

$$\mathbf{y}(t) = \mathbf{F}(t; \mathbf{y}^o, t^o) + \mathbf{w}(t). \quad (44)$$

This equation admits an equivalent discrete-time representation that describes how the solution advances from t^k to t^{k+1} :

$$\mathbf{y}^{k+1} = \mathbf{F}(t^{k+1}; \mathbf{y}^k, t^k) + \mathbf{w}^k. \quad (45)$$

Observations of the state of the system, \mathbf{z} , are given by the measurement function \mathbf{h} and the observation error \mathbf{v} :

$$\mathbf{z}^{k+1} = \mathbf{h}(\mathbf{y}^{k+1}) + \mathbf{v}^{k+1} \quad (46)$$

Both the process and measurement noises are assumed Gaussian with zero mean, noncorrelated (i.e. $\mathbb{E}[\mathbf{v}^k(\mathbf{w}^\ell)^\top] = 0$ for all k, ℓ), and

$$\mathbb{E}[\mathbf{w}^k(\mathbf{w}^\ell)^\top] = \begin{cases} \mathbf{0}, & \text{if } k \neq \ell \\ \mathbf{Q}^k, & \text{if } k = \ell \end{cases}; \quad \mathbb{E}[\mathbf{v}^k(\mathbf{v}^\ell)^\top] = \begin{cases} \mathbf{0}, & \text{if } k \neq \ell \\ \mathbf{R}^k, & \text{if } k = \ell \end{cases} \quad (47)$$

The matrices \mathbf{Q}^k and \mathbf{R}^k are the covariance matrices associated with the process and measurement noises, respectively.

The Kalman filter algorithm [16] comprises two steps: prediction and update. In a general setting, the mean and covariance of the posterior distribution can be predicted from the expressions:

$$\hat{\mathbf{m}}^{k+1} = \mathbb{E}[\mathbf{F}(t^{k+1}; \bar{\mathbf{y}}^k, t^k) + \mathbf{w}^k | \mathbf{z}^k] \quad (48)$$

$$\hat{\mathbf{P}}^{k+1} = \mathbb{E}\{[\mathbf{F}(t^{k+1}; \bar{\mathbf{y}}^k, t^k) + \mathbf{w}^k][\mathbf{F}(t^{k+1}; \bar{\mathbf{y}}^k, t^k) + \mathbf{w}^k]^\top | \mathbf{z}^k\} - \hat{\mathbf{m}}^{k+1}(\hat{\mathbf{m}}^{k+1})^\top \quad (49)$$

The symbol $\hat{\cdot}$ denotes predicted values and $\bar{\cdot}$ denotes updated values. Similarly, one can compute the expectation of the observations from Eq. (46):

$$\hat{\mathbf{h}}^{k+1} = \mathbb{E}[\mathbf{h}(\bar{\mathbf{y}}^{k+1}) + \mathbf{v}^{k+1} | \mathbf{z}^k]. \quad (50)$$

The optimal Kalman gain at t^{k+1} reads

$$\mathbf{K}^{k+1} = (\mathbf{P}^{\mathbf{y}\mathbf{z}})^{k+1} [(\mathbf{P}^{\mathbf{z}\mathbf{z}})^{k+1}]^{-1} \quad (51)$$

where $(\mathbf{P}^{yz})^{k+1}$ and $(\mathbf{P}^{zz})^{k+1}$ are the cross-covariance matrix of state and observations and the covariance matrix of the observations, respectively, computed at time t^{k+1} . They are defined as:

$$(\mathbf{P}^{yz})^{k+1} = \mathbb{E}[(\hat{\mathbf{y}}^{k+1} - \hat{\mathbf{m}}^{k+1})(\hat{\mathbf{z}}^{k+1} - \hat{\mathbf{n}}^{k+1})^\top] \quad (52)$$

$$(\mathbf{P}^{zz})^{k+1} = \mathbb{E}[(\hat{\mathbf{z}}^{k+1} - \hat{\mathbf{n}}^{k+1})(\hat{\mathbf{z}}^{k+1} - \hat{\mathbf{n}}^{k+1})^\top] \quad (53)$$

The updated values of the mean and the covariance are obtained from the predicted ones according to

$$\bar{\mathbf{m}}^{k+1} = \hat{\mathbf{m}}^{k+1} + \mathbf{K}^{k+1}(\mathbf{z}^{k+1} - \hat{\mathbf{n}}^{k+1}) \quad (54)$$

$$\bar{\mathbf{P}}^{k+1} = \hat{\mathbf{P}}^{k+1} - \mathbf{K}^{k+1}(\mathbf{P}^{zz})^{k+1}(\mathbf{K}^{k+1})^\top \quad (55)$$

The term $(\mathbf{z}^{k+1} - \hat{\mathbf{n}}^{k+1})$ is the residual of the observation at t^{k+1} .

A. Linear Kalman Filter (LKF)

Assuming that the dynamical system (1) can be linearized about a reference solution, the Kalman filter simplifies to the linear Kalman filter (LKF). The reference trajectory is integrated at once before running the filter and the LKF fits the deviations from the reference to the data. The equations that predict the evolution of the deviation $\delta\mathbf{y}$ and the covariance matrix are:

$$\delta\hat{\mathbf{y}}^{k+1} = \Phi(t^k, t^{k+1})\delta\bar{\mathbf{y}}^k \quad (56)$$

$$\hat{\mathbf{P}}^{k+1} = \Phi(t^k, t^{k+1})\bar{\mathbf{P}}^k[\Phi(t^k, t^{k+1})]^\top + \mathbf{Q}^k \quad (57)$$

The prediction is then updated according to

$$\delta\bar{\mathbf{y}}^{k+1} = \delta\hat{\mathbf{y}}^{k+1} + \mathbf{K}^{k+1}(\mathbf{z}^{k+1} - \mathbf{H}^{k+1}\delta\hat{\mathbf{y}}^{k+1}) \quad (58)$$

$$\bar{\mathbf{P}}^{k+1} = (\mathbf{I} - \mathbf{K}^{k+1}\mathbf{H}^{k+1})\hat{\mathbf{P}}^{k+1} \quad (59)$$

where \mathbf{H} is the matrix of partial derivatives of the observation function with respect to the state variables:

$$H_{ij} = \frac{\partial h_i}{\partial x_j} \quad (60)$$

The computation of the Kalman gain in Eq. (51) reduces to:

$$\mathbf{K}^{k+1} = \hat{\mathbf{P}}^{k+1}(\mathbf{H}^{k+1})^\top [\mathbf{H}^{k+1}\hat{\mathbf{P}}^{k+1}(\mathbf{H}^{k+1})^\top + \mathbf{R}^{k+1}]^{-1} \quad (61)$$

B. Extended Kalman filter (EKF)

The extended Kalman filter (EKF) improves upon the LKF thanks to a more accurate prediction of the state and state-transition matrix at t^{k+1} . The prediction consists in propagating the variational equations of motion from t^k to t^{k+1} starting from the updated value of the mean $\bar{\mathbf{m}}^k$ obtained in the previous step, which then leads to the predicted value of the observation $\hat{\mathbf{n}}^{k+1}$:

$$\hat{\mathbf{m}}^{k+1} = \mathbf{F}(t^{k+1}; \bar{\mathbf{m}}^k, t^k) \quad (62)$$

$$\hat{\mathbf{n}}^{k+1} = \mathbf{h}(\hat{\mathbf{m}}^{k+1}) \quad (63)$$

The covariance matrix is predicted using Eq. (57). The mean is updated with

$$\bar{\mathbf{m}}^{k+1} = \hat{\mathbf{m}}^{k+1} + \mathbf{K}^{k+1}(\mathbf{z}^{k+1} - \hat{\mathbf{n}}^{k+1}) \quad (64)$$

and the covariance matrix is updated with Eq. (59).

C. Unscented Kalman Filter (UKF)

The propagation of the first and second moments of the distribution in the EKF is limited in the sense that it neglects the contribution from the higher-order moments. For example, the predicted value of the mean of the posterior distribution is simply the propagated value of the mean of the prior. To propagate the probability distribution and accurately predict the moments of the posterior distribution, a possibility is to resort to MC sampling following the particle-filter model. The unscented Kalman filter (UKF) [1, 2] avoids the propagation of thousands of MC samples by sampling only the sigma points. The UKF algorithm predicts the future value of the mean and covariance by first integrating the sigma points forward in time in the fully nonlinear dynamical model and then computing the mean and covariance of the propagated sigma points. Thanks to capturing the deviations of the mean and covariance caused by the higher-order moments of the distribution, UKF proves to be a reliable and more accurate alternative to EKF in most practical scenarios.

D. High-order Approximate Extended Kalman Filter (HApEKF)

Instead of propagating a set of MC samples or a set of sigma points, Park and Scheeres [7] suggested a technique to capture the effects of high-order moments relying on Taylor expansions of the expectations in Eqs. (48–50) and (52–53). Let $\mathbf{y}^k = \mathbf{m}^k + \delta \mathbf{y}^k$ denote the true state at t^k and $\delta \mathbf{y}^k$ the deviation from the mean. Introducing this expression into the aforementioned equations and expanding in series around the mean value using the STTs in Eq. (7) provides the prediction of the mean and covariance:

$$\begin{aligned}\hat{m}_i^{k+1} &= \mathbb{E}[F_i(t^{k+1}; \bar{\mathbf{m}}^k + \delta \mathbf{y}^k, t^k) + w_i^k] = F_i(t^{k+1}; \bar{\mathbf{m}}^k, t^k) + \delta m_i^{k+1} \\ &= F_i(t^{k+1}; \bar{\mathbf{m}}^k, t^k) + \sum_{p=1}^m \frac{1}{p!} \Phi_{i, \gamma_1 \dots \gamma_p}^{(t^k, t^{k+1})} \mathbb{E}[\delta y_{\gamma_1}^k \dots \delta y_{\gamma_p}^k]\end{aligned}\quad (65)$$

$$\begin{aligned}\hat{\mathbf{P}}_{ij}^{k+1} &= \mathbb{E}\{[F_i(t^{k+1}; \bar{\mathbf{m}}^k + \delta \mathbf{y}^k, t^k) + w_i^k][F_j(t^{k+1}; \bar{\mathbf{m}}^k + \delta \mathbf{y}^k, t^k) + w_j^k]\} - \hat{m}_i^{k+1} \hat{m}_j^{k+1} \\ &= \sum_{p=1}^m \sum_{q=1}^m \frac{1}{p!q!} \Phi_{i, \gamma_1 \dots \gamma_p}^{(t^k, t^{k+1})} \Phi_{j, \zeta_1 \dots \zeta_q}^{(t^k, t^{k+1})} \mathbb{E}[\delta y_{\gamma_1}^k \dots \delta y_{\gamma_p}^k \delta y_{\zeta_1}^k \dots \delta y_{\zeta_q}^k] - \delta m_i^{k+1} \delta m_j^{k+1} + Q_{ij}^k\end{aligned}\quad (66)$$

Similarly, the predicted values of the observations and the covariance matrices \mathbf{P}^{yz} and \mathbf{P}^{zz} read

$$\hat{n}_i^{k+1} = \mathbb{E}[h_i(\bar{\mathbf{m}}^k + \delta \mathbf{y}^k) + v_i^{k+1}] = h_i(\bar{\mathbf{m}}^k) + \delta n_i^{k+1} = h_i(\bar{\mathbf{m}}^k) + \sum_{p=1}^m \frac{1}{p!} \Xi_{i, \gamma_1 \dots \gamma_p}^{(t^k, t^{k+1})} \mathbb{E}[\delta y_{\gamma_1}^k \dots \delta y_{\gamma_p}^k]\quad (67)$$

$$\begin{aligned}(P_{ij}^{yz})^{k+1} &= \mathbb{E}[\hat{y}_i^{k+1} \hat{z}_j^{k+1}] - \hat{m}_i^{k+1} \hat{n}_j^{k+1} \\ &= \mathbb{E}\{[F_i(\bar{\mathbf{m}}^k + \delta \mathbf{y}^k) + w_i^{k+1}][h_j(\bar{\mathbf{m}}^k + \delta \mathbf{y}^k) + v_j^{k+1}]\} - \hat{m}_i^{k+1} \hat{n}_j^{k+1} \\ &= \sum_{p=1}^m \sum_{q=1}^m \frac{1}{p!q!} \Phi_{i, \gamma_1 \dots \gamma_p}^{(t^k, t^{k+1})} \Xi_{j, \zeta_1 \dots \zeta_q}^{(t^k, t^{k+1})} \mathbb{E}[\delta y_{\gamma_1}^k \dots \delta y_{\gamma_p}^k \delta y_{\zeta_1}^k \dots \delta y_{\zeta_q}^k] + R_{ij}^{k+1} - \delta m_i^{k+1} \delta n_j^{k+1}\end{aligned}\quad (68)$$

$$\begin{aligned}(P_{ij}^{zz})^{k+1} &= \mathbb{E}[\hat{z}_i^{k+1} \hat{z}_j^{k+1}] - \hat{n}_i^{k+1} \hat{n}_j^{k+1} \\ &= \mathbb{E}\{[h_i(\bar{\mathbf{m}}^k + \delta \mathbf{y}^k) + v_i^{k+1}][h_j(\bar{\mathbf{m}}^k + \delta \mathbf{y}^k) + v_j^{k+1}]\} - \hat{n}_i^{k+1} \hat{n}_j^{k+1} \\ &= \sum_{p=1}^m \sum_{q=1}^m \frac{1}{p!q!} \Xi_{i, \gamma_1 \dots \gamma_p}^{(t^k, t^{k+1})} \Xi_{j, \zeta_1 \dots \zeta_q}^{(t^k, t^{k+1})} \mathbb{E}[\delta y_{\gamma_1}^k \dots \delta y_{\gamma_p}^k \delta y_{\zeta_1}^k \dots \delta y_{\zeta_q}^k] + R_{ij}^{k+1} - \delta n_i^{k+1} \delta n_j^{k+1}\end{aligned}\quad (69)$$

Equations (67–69) have been written in terms of the tensor

$$\Xi_{i, \gamma_1 \dots \gamma_p}^{(t^k, t^{k+1})} = \frac{\partial^p h_i(\mathbf{y}^{k+1})}{\partial y_{\gamma_1}^k \dots \partial y_{\gamma_p}^k}\quad (70)$$

which accounts for both the sensitivity of the observation function to changes in the state vector and the sensitivity of the state at t^{k+1} to changes in the initial conditions at t^k . Introducing the auxiliary tensor

$$H_{i, \gamma_1 \dots \gamma_p} = \frac{\partial^p h_i(\mathbf{y}^{k+1})}{\partial y_{\gamma_1}^{k+1} \dots \partial y_{\gamma_p}^{k+1}}\quad (71)$$

the simple case $p = 1$ reduces to

$$\Xi_{i,a}^{(t^k, t^{k+1})} = H_{i,\alpha} \Phi_{\alpha,a}^{(t^k, t^{k+1})} \implies \Xi^{(t^k, t^{k+1})} = \mathbf{H} \Phi^{(t^k, t^{k+1})}. \quad (72)$$

For second order, the chain rule provides:

$$\Xi_{i,ab}^{(t^k, t^{k+1})} = H_{i,\alpha} \Phi_{\alpha,ab}^{(t^k, t^{k+1})} + H_{i,\alpha\beta} \Phi_{\alpha,a}^{(t^k, t^{k+1})} \Phi_{\beta,b}^{(t^k, t^{k+1})} \quad (73)$$

The update equations are the standard ones from the Kalman filter algorithm:

$$\mathbf{K}^{k+1} = (\mathbf{P}^{\mathbf{y}\mathbf{z}})^{k+1} [(\mathbf{P}^{\mathbf{z}\mathbf{z}})^{k+1}]^{-1} \quad (74)$$

$$\bar{\mathbf{m}}^{k+1} = \hat{\mathbf{m}}^{k+1} + \mathbf{K}^{k+1} (\mathbf{z}^{k+1} - \hat{\mathbf{n}}^{k+1}) \quad (75)$$

$$\bar{\mathbf{P}}^{k+1} = \hat{\mathbf{P}}^{k+1} - \mathbf{K}^{k+1} (\mathbf{P}^{\mathbf{z}\mathbf{z}})^{k+1} (\mathbf{K}^{k+1})^\top \quad (76)$$

E. Examples

Two examples of trajectory estimation problems are proposed to study the performance of the HApEKF algorithm compared to LKF, EKF, and UKF. We investigate the relative performance of the filter when dealing both with linear and nonlinear measurement models.

1. Europa orbiter

Consider a hypothetical spacecraft orbiting Europa. The osculating orbital elements at the initial epoch are defined in Table 4. The orbit is slightly eccentric with a periapsis altitude of 240 km. The perturbations included in the dynamical model are the strong gravitational attraction from Jupiter and the effect of the J_2 -term of Europa's gravity field.

Table 4 Osculating orbital elements of an Europa orbiter in the ecliptic frame.

a (km)	e	i (deg)	Ω (deg)	ω (deg)	M (deg)
2000	0.1	40	0	40	0

The observation model simulates readings from radar altimetry and landmark navigation, providing measurements of the radial distance to Europa, the latitude and longitude of the sub-spacecraft point, and the range rate. Measurement errors are modeled with Gaussian distributions with zero mean and no cross correlation. The standard deviation of the radial measurement is $\sigma_r = 10$ km, of the angular measurements is $\sigma_\alpha = \sigma_\delta = 10^{-3}$, and of the range rate is $\sigma_{\dot{r}} = 1$ m/s. The initial orbital uncertainty is $\sigma_x = \sigma_y = \sigma_z = 10$ km in position and $\sigma_{v_x} = \sigma_{v_y} = \sigma_{v_z} = 1$ m/s in velocity. Measurements are available only twice per orbit. In this example and the one that follows, the process noise is neglected under the assumption that all forces acting on the spacecraft are accounted for in the force model.

Under these assumptions and with the referred measurement model, Fig. 8 presents the errors in the orbital estimates using LKF, EKF, HApEKF (with $m = 2$), and UKF, together with the evolution of the uncertainties. The solution predicted by the LKF method diverges and it quickly gets out-of-scale in Fig. 8a. Although the uncertainties are reduced to about 1 km in position and 0.01 m/s in velocity (Fig. 8b), the limitations in the physical model and the update steps prevent the algorithm from converging to a more accurate solution. EKF also struggles to converge partially due to the low frequency of the measurements. HApEKF ($m = 2$) adequately accounts for the contributions of the higher-order moments of the probability distribution and reduces the final errors in position and velocity by one order of magnitude compared to EKF. It matches the accuracy of UKF thanks to a refined update of the mean and covariance of the distribution based on Eqs. (67–69). Given the nonlinear nature of the measurement model, retaining terms of second order when estimating the residuals of the observations and computing the optimal Kalman gain has a significant impact on the solution.

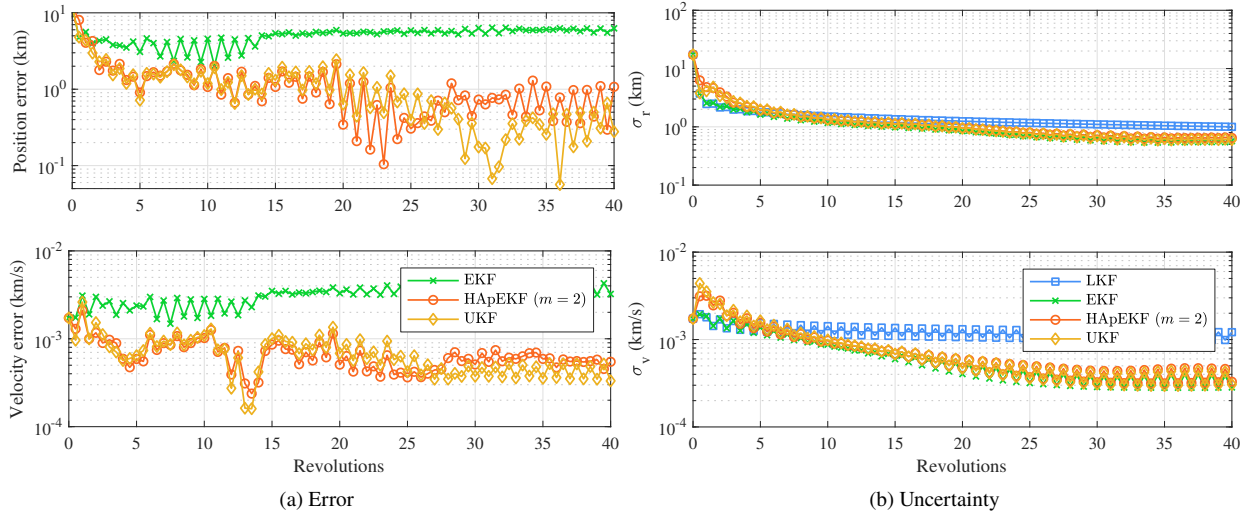


Fig. 8 Comparison of the errors and uncertainties in position and velocity obtained with LKF, EKF, HApEKF ($m = 2$), and UKF for the case of an Europa orbiter. Nonlinear measurement model with range-rate data.

To analyze the robustness of HApEKF ($m = 2$) when dealing with more limited observations, let us assume that range-rate measurements are no longer available. The observational data does not provide direct measurements of the radial velocity of the spacecraft, only of its distance to Europa and its angular position. Figure 9a indicates that EKF fails to converge in this scenario and results in errors in position and velocity that are larger than the initial errors. The divergence of EKF is caused by a subestimation of the position uncertainty that makes the filter value the residuals more than it should ideally do. Conversely, the higher-order HApEKF ($m = 2$) remains accurate to the sub-kilometer level in position and sub-meter-per-second in velocity, which is comparable to the UKF estimation.

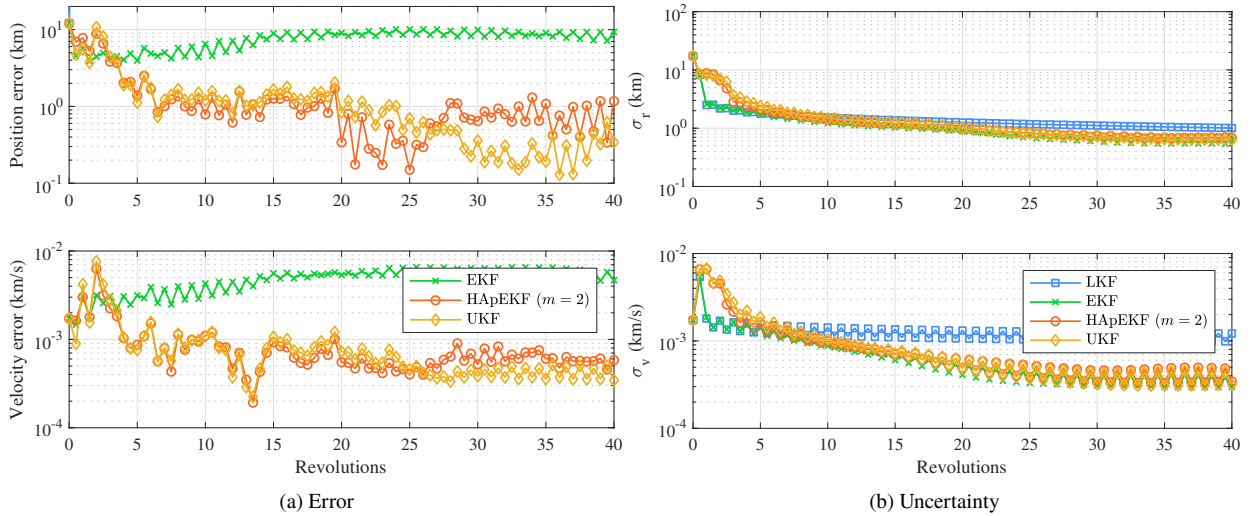


Fig. 9 Comparison of the errors and uncertainties in position and velocity obtained with LKF, EKF, HApEKF ($m = 2$), and UKF for the case of an Europa orbiter. Nonlinear measurement model without range-rate data.

2. Spacecraft in low-Earth orbit

Consider the low-Earth orbit defined in Table 3. The orbital perturbations account for the effect of Earth's J_2 and the gravitational attraction from the Sun and the Moon. To test the performance of the nonlinear filter, consider a set of

fictitious measurements taken every 0.2 revolutions, equivalent to 20 minutes. The measurement model simulates very long base interferometry (VLBI) readings by providing the values of the y -component of the position vector on the inertial frame. Consequently, the measurement model is linear and the high-order partial derivatives of the measurement function are zero. The error in the measurements is assumed Gaussian with zero mean and standard deviation of 1 m. The initial orbital uncertainties are $\sigma_x = \sigma_y = \sigma_z = 1$ km in position and $\sigma_{v_x} = \sigma_{v_y} = \sigma_{v_z} = 1$ m/s in velocity.

Figure 10 compares the accuracy of LKF, EKF, HApEKF (second order), and UKF when filtering the data. The methods are compared in terms of the error in position and velocity. The linear filter diverges over time and the error grows to several hundreds of kilometers in position and approximately 1 km/s in velocity (see Fig. 10a). The estimate from the EKF algorithm is accurate to 1 km and slowly improves over time. Including second-order terms using HApEKF results in a converged solution that is approximately one order of magnitude more accurate than the standard EKF. The accuracy of the HApEKF matches that of the UKF both in position and velocity.

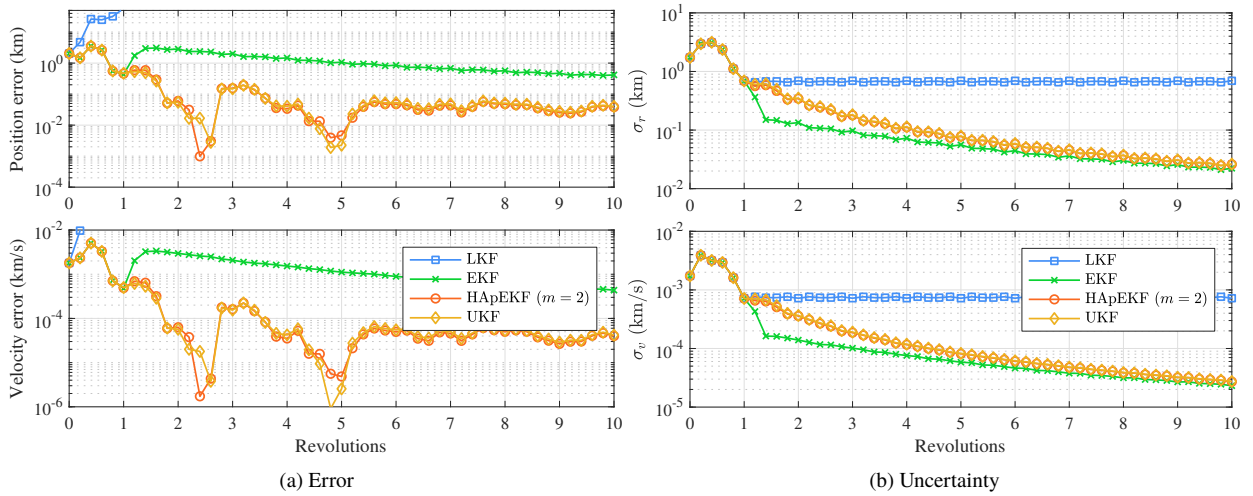


Fig. 10 Comparison of the errors and uncertainties in position and velocity obtained with LKF, EKF, HApEKF ($m = 2$), and UKF for the case of a spacecraft in low-Earth orbit with small uncertainties and linear measurement model.

The analysis of the uncertainty presented in Fig. 10b indicates that EKF reduces the uncertainty too rapidly and, as a result, it underestimates the information from the observations. The uncertainty predicted by HApEKF and UKF exhibits a similar smooth trend.

Next, we increase the initial orbital uncertainty to $\sigma_x = \sigma_y = \sigma_z = 100$ km and $\sigma_{v_x} = \sigma_{v_y} = \sigma_{v_z} = 5$ m/s to test the robustness of the filter. Similarly, the standard deviation of the measurements is increased to 100 m. The larger uncertainties in the orbit and the measurements cause the LKF algorithm to diverge after merely one revolution and the EKF method to stall at an error of 100 km in position and 100 m/s in velocity, as shown in Fig. 11a. The rapid reduction of the uncertainty is responsible for EKF not being able to further improve the solution. Conversely, the improved estimation of the first and second moments of the posterior distribution provided by HApEKF results in a prediction that is as accurate as the UKF solution without the need for integrating numerically several samples.

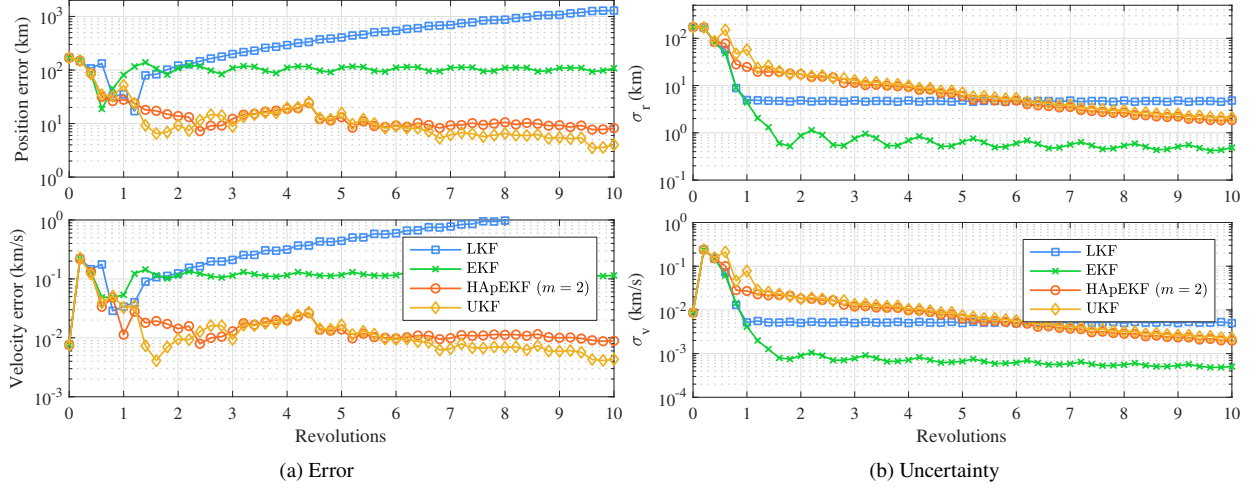


Fig. 11 Comparison of the errors and uncertainties in position and velocity obtained with LKF, EKF, HApEKF ($m = 2$), and UKF for the case of a spacecraft in low-Earth orbit with large uncertainties.

V. Conclusions

The technique presented in this paper provides a simple yet accurate nonlinear method for uncertainty propagation by approximating high-order STTs. Thanks to capturing the dominant nonlinear effects, this technique efficiently models the evolution of the first and second moments of the initial probability distribution. The method is not restricted to any particular force model or application, and the examples presented herein show how the method can handle typical orbital perturbations. The main advantage of the method is the simplicity of its implementation compared to integrating the corresponding high-order variational equations.

Furthermore, the approximation of the high-order STTs can be exploited to formulate a high-order version of the extended Kalman filter (EKF). Thanks to capturing the contribution from the high-order moments when estimating the mean and covariance of the posterior distribution, the proposed version of EKF becomes as accurate as the unscented Kalman filter, with the advantage of not needing to numerically integrate the evolution of the sigma points.

The proposed method is particularly useful for approximating the second-order STT. With only seven additional equations required to produce the approximation, the resulting formulation is substantially less computationally intensive than the propagation of the full second-order STT. The accuracy of the approximation for uncertainty propagation is comparable to the accuracy of the unscented transform, and the evaluation of the series is more efficient than the numerical integration of the sigma points.

Acknowledgments

This work was carried out at the Jet Propulsion Laboratory, California Institute of Technology, under a contract with the National Aeronautics and Space Administration (80NM0018D004).

Appendix: time derivatives of the acceleration

The approximation of the STTs in Eq. (21) requires the time derivatives of the solution, $d^i \mathbf{F}/dt^i$. Equations (1) and (2) readily provide

$$\frac{d\mathbf{F}}{dt} \equiv \mathbf{f} = \begin{bmatrix} \mathbf{v} \\ \mathbf{a} \end{bmatrix}, \quad (77)$$

where the total acceleration

$$\mathbf{a} = -\frac{\mu}{r^3} \mathbf{r} + \mathbf{a}_p = \mathbf{a}_k + \mathbf{a}_p \quad (78)$$

decomposes in the Keplerian acceleration \mathbf{a}_k plus the perturbation \mathbf{a}_p . Higher derivatives of \mathbf{F} involve the acceleration and its time derivative, the jerk $\dot{\mathbf{a}}$:

$$\frac{d\mathbf{v}}{dt} = \mathbf{a}, \quad \frac{d\mathbf{a}}{dt} = \dot{\mathbf{a}}. \quad (79)$$

A. Kepler's problem

The time derivative of the Keplerian acceleration takes the form:

$$\dot{\mathbf{a}}_k = \frac{\mu}{r^5} \left[3(\mathbf{v} \cdot \mathbf{r}) \mathbf{r} - r^2 \mathbf{v} \right] \quad (80)$$

where \mathbf{I} is the 3×3 identity matrix. It is then easy to write the derivatives of the solution \mathbf{F} like

$$\frac{d\mathbf{F}_k}{dt} = \begin{bmatrix} \mathbf{v} \\ \mathbf{a}_k \end{bmatrix}, \quad \frac{d^2\mathbf{F}_k}{dt^2} = \begin{bmatrix} \mathbf{a}_k \\ \dot{\mathbf{a}}_k \end{bmatrix}. \quad (81)$$

B. Third-body perturbation

Let \mathbf{r}_i denote the position of a perturbing body i with gravitational parameter μ_i , and \mathbf{r}_{rel} the relative separation $\mathbf{r}_{\text{rel}} = \mathbf{r} - \mathbf{r}_i$. The third-body perturbation due to body i is

$$\mathbf{a}_{3b} = -\mu_i \left(\frac{\mathbf{r}_{\text{rel}}}{r_{\text{rel}}^3} + \frac{\mathbf{r}_i}{r_i^3} \right) \equiv \mathbf{a}_{\text{rel}} + \mathbf{a}_i. \quad (82)$$

The derivative of the perturbation is

$$\frac{d\mathbf{a}_{3b}}{dt} = \dot{\mathbf{a}}_{\text{rel}} + \dot{\mathbf{a}}_i \quad (83)$$

and can be obtained by replacing μ with μ_i and $\{\mathbf{r}, \mathbf{v}, \mathbf{a}\}$ with $\{\mathbf{r}_{\text{rel}}, \mathbf{v}_{\text{rel}}, \mathbf{a}_{\text{rel}}\}$ and $\{\mathbf{r}_i, \mathbf{v}_i, \mathbf{a}_i\}$ in Eq. (80). The contributions to the derivatives in Eq. (81) are

$$\frac{d\mathbf{F}_{3b}}{dt} = \begin{bmatrix} 0 \\ \mathbf{a}_{3b} \end{bmatrix}, \quad \frac{d^2\mathbf{F}_{3b}}{dt^2} = \begin{bmatrix} \mathbf{a}_{3b} \\ \dot{\mathbf{a}}_{3b} \end{bmatrix}. \quad (84)$$

The velocity \mathbf{v}_i and acceleration \mathbf{a}_i are the velocity and acceleration of the i -th body with respect to the central body, whereas $\mathbf{v}_{\text{rel}} = \mathbf{v} - \mathbf{v}_i$ and $\mathbf{a}_{\text{rel}} = \mathbf{a} - \mathbf{a}_i$. When the states of the perturbing bodies are retrieved from a set of numerical ephemerides, the acceleration \mathbf{a}_i is computed numerically unless the high-order derivatives of the interpolating functions are available.

C. J_2 perturbation

The perturbation caused by the oblateness of the central body is typically written using coordinates in a body-fixed frame, denoted with the subscript b , and in terms of the constant parameter $\alpha = J_2 \mu R_{\text{eq}}^2$. It reads:

$$\mathbf{a}_{J_2} = -\frac{3}{2} \frac{\alpha}{r^7} \begin{bmatrix} x_b(r^2 - 5z_b^2) \\ y_b(r^2 - 5z_b^2) \\ z_b(3r^2 - 5z_b^2) \end{bmatrix}. \quad (85)$$

The jerk can be computed in two steps like

$$\frac{d\mathbf{a}_{J_2}}{dt} \equiv \dot{\mathbf{a}}_{J_2} = \frac{\partial \mathbf{a}_{J_2}}{\partial \mathbf{r}_b} \mathbf{v}_b + \frac{1}{r} \frac{\partial \mathbf{a}_{J_2}}{\partial r} (\mathbf{v}_b \cdot \mathbf{r}_b). \quad (86)$$

The derivatives in Eq. (86) take the form:

$$\begin{aligned} \frac{\partial \mathbf{a}_{J_2}}{\partial \mathbf{r}_b} &= -\frac{3}{2} \frac{\alpha}{r^7} \begin{bmatrix} (r^2 - 5z_b^2) & 0 & -10x_b z_b \\ 0 & (r^2 - 5z_b^2) & -10y_b z_b \\ 0 & 0 & 3(r^2 - 5z_b^2) \end{bmatrix} \\ \frac{\partial \mathbf{a}_{J_2}}{\partial r} &= \frac{15}{2} \frac{\alpha}{r^8} \begin{bmatrix} x_b(r^2 - 7z_b^2) \\ y_b(r^2 - 7z_b^2) \\ z_b(3r^2 - 7z_b^2) \end{bmatrix} \end{aligned} \quad (87)$$

D. Solar radiation pressure

Assuming that the reflective area of the body is normal to the Sun direction, the acceleration due to the solar radiation simplifies to

$$\mathbf{a}_{\text{srp}} = -\Phi c_R \frac{A}{m} \frac{\mathbf{r}_s}{r_s^3} \equiv -\beta \frac{\mathbf{r}_s}{r_s^3}. \quad (88)$$

The area-to-mass ratio A/m , the reflectivity coefficient c_R , and the solar flux Φ are assumed constant. Consequently, $\beta = \Phi c_R A/m$ is constant too. Vector \mathbf{r}_s denotes the position of the Sun relative to the body. The jerk follows from Eq. (80) simply by replacing μ with β and $\{\mathbf{r}, \mathbf{v}\}$ with $\{\mathbf{r}_s, \mathbf{v}_s\}$:

$$\dot{\mathbf{a}}_{\text{srp}} = \frac{\beta}{r_s^5} \left[3(\mathbf{v}_s \cdot \mathbf{r}_s) \mathbf{r}_s - r_s^2 \mathbf{v}_s \right]. \quad (89)$$

The relative acceleration is $\mathbf{a}_s = \mathbf{a}_\odot - \mathbf{a}$, where \mathbf{a}_\odot denotes the acceleration of the Sun relative to the center of attraction.

References

- [1] Julier, S. J., Uhlmann, J. K., and Durrant-Whyte, H. F., “A new approach for filtering nonlinear systems,” *Proceedings of 1995 American Control Conference-ACC’95*, Vol. 3, IEEE, 1995, pp. 1628–1632.
- [2] Julier, S. J., and Uhlmann, J. K., “Unscented filtering and nonlinear estimation,” *Proceedings of the IEEE*, Vol. 92, No. 3, 2004, pp. 401–422.
- [3] Terejanu, G., Singla, P., Singh, T., and Scott, P. D., “Uncertainty propagation for nonlinear dynamic systems using Gaussian mixture models,” *Journal of Guidance, Control, and Dynamics*, Vol. 31, No. 6, 2008, pp. 1623–1633.
- [4] Jones, B. A., Doostan, A., and Born, G. H., “Nonlinear propagation of orbit uncertainty using non-intrusive polynomial chaos,” *Journal of Guidance, Control, and Dynamics*, Vol. 36, No. 2, 2013, pp. 430–444.
- [5] Park, R. S., and Scheeres, D. J., “Nonlinear mapping of Gaussian statistics: theory and applications to spacecraft trajectory design,” *Journal of Guidance, Control, and Dynamics*, Vol. 29, No. 6, 2006, pp. 1367–1375.
- [6] Arulampalam, M. S., Maskell, S., Gordon, N., and Clapp, T., “A tutorial on particle filters for online nonlinear/non-Gaussian Bayesian tracking,” *IEEE Transactions on Signal Processing*, Vol. 50, No. 2, 2002, pp. 174–188.
- [7] Park, R. S., and Scheeres, D. J., “Nonlinear semi-analytic methods for trajectory estimation,” *Journal of Guidance, Control, and Dynamics*, Vol. 30, No. 6, 2007, pp. 1668–1676.
- [8] Nayfeh, A. H., *Perturbation methods*, John Wiley & Sons, 2008.
- [9] Baumgarte, J., and Stiefel, E., “Examples of transformations improving the numerical accuracy of the integration of differential equations,” *Proceedings of the Conference on the Numerical Solution of Ordinary Differential Equations*, Springer, 1974, pp. 207–236.
- [10] Baumgarte, J., “Stabilized Kepler motion connected with analytic step adaptation,” *Celestial Mechanics*, Vol. 13, No. 1, 1976, pp. 105–109.
- [11] Roa, J., *Regularization in Orbital Mechanics: Theory and Practice*, Vol. 42, Walter de Gruyter GmbH & Co KG, 2017.
- [12] Szebehely, V., *Theory of orbits: the restricted problem of three bodies*, New York: Academic Press, 1967.
- [13] Hiday-Johnston, L., and Howell, K., “Transfers between libration-point orbits in the elliptic restricted problem,” *Celestial Mechanics and Dynamical Astronomy*, Vol. 58, No. 4, 1994, pp. 317–337.
- [14] Roa, J., and Peláez, J., “The theory of asynchronous relative motion I: time transformations and nonlinear corrections,” *Celestial Mechanics and Dynamical Astronomy*, Vol. 127, No. 3, 2017, pp. 301–330.
- [15] Roa, J., and Peláez, J., “The theory of asynchronous relative motion II: universal and regular solutions,” *Celestial Mechanics and Dynamical Astronomy*, Vol. 127, No. 3, 2017, pp. 343–368.
- [16] Kalman, R. E., “A new approach to linear filtering and prediction problems,” *Journal of basic Engineering*, Vol. 82, No. 1, 1960, pp. 35–45.